Proc Indian Natn Sci Acad **79** No. 4 December 2013 Spl. Issue, Part A, pp. 735-743

Research Paper

Hypervelocity Impact of Steel Microsphere on Glass Sheet

A CHADEGANI and R C BATRA*
Department of Engineering Science and Mechanics, M/C 0219, Virginia Polytechnic Institute and State University, Blacksburg, VA 24061 USA

(Received 28 April 2013; Accepted 30 April 2013)

We use the smooth particle hydrodynamics formulation implemented in the commercial software AUTODYN to analyze axisymmetric deformations due to the high speed impact at normal incidence of a glass sheet by a steel sphere. We compare computed values of the conchoidal diameters on the front and the back surfaces and the hole-out diameter with their experimental values available in the literature and also with those computed by Michel *et al.* for the same problem. The steel and the glass are modelled, respectively, with the Johnson-Cook and the Johnson-Holmquist thermoelastoviscoplastic relations and the Mie-Grüneisen and the polynomial equations of state. It is found that the agreement between the computed and the test results improves with an increase in the impact speed, and our results differ from those of Michel *et al.* who used the SPH formulation implemented in the commercial code LSDYNA.

Key Words: Hypervelocity Impact; Smooth Particle Hydrodynamics; Thermoelastoviscoplasticity; Spall Failure; Crater Diameter; Conchoidal Diameter

1. Introduction

Impacts in which pressures induced are an order of magnitude greater than the projectile and the target strength are usually termed as hypervelocity impacts (HVIs). Damage evolved during HVIs depends upon the materials of the impactor and the target, the impact speed and the initial and the boundary conditions. For example, damage in glass shown in Fig. 1, taken from Ref. [1], is different from that in ductile and even brittle metallic targets. Even though the initial impact pressure generated by HVI on glass is not much less than that on aluminum, the damage is much more extensive. Whereas the front-surface conchoidal diameter, D_s, in brittle aluminum is slightly larger than the crater diameter, D_c, and is about 4 times the projectile diameter, d_p, in glass $D_s \approx 40\, d_p$ and $D_c \approx 10\, d_p$. This is believed to be due to the low tensile strength of glass as compared to that of aluminum [2]. The shock pressure produced by a HVI is much larger than the tensile strength of glass and tensile stresses released on reflections from the free surfaces dominate the material strength for a long time. Therefore, a glass target must be much thicker than the aluminum counterpart to prevent spall failure [2] for otherwise identical impact conditions.

Laboratory experiments are expensive, and in general controlled tests cannot be performed for establishing an optimum design. Hydrocodes (e.g., AUTODYN, LSDYNA, and ABAQUS) on the other hand used to solve initial-boundary-value problems (IBVPs) employ established mechanics principles, i.e., the conservations of mass, linear momentum, and energy. However, there is no consensus on the failure criteria and their implementations in hydrocodes. Computed results depend upon these factors, constitutive relations used to describe the material response at high strain rates and temperatures, values of material parameters derived from either test data or results of molecular mechanics simulations, and algorithms used to simulate non-interpenetration

*Authors for Correspondence: E-mail: rbatra@vt.edu, chadegan@vt.edu

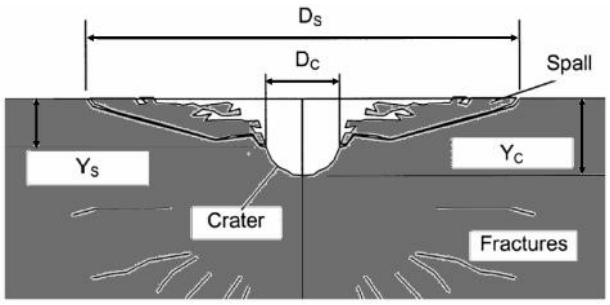

Fig. 1: Schematic sketch of the damage evolved in fused silica glass [1]

conditions between two contacting bodies. Hydrocodes are economical to use and help conduct sensitivity studies to determine the importance of different parameters. It is rather well known that different hydrocodes using the same material models and values of material parameters can give quite different results. Here we have used the smoothed particle hydrodynamics (SPH) formulation included in the commercial software AUTODYN [3] to analyze finite deformations and failure of a glass plate impacted at normal incidence by a steel sphere, and compared our results with those of Michel *et al.* [4-6] who also used the SPH formulation implemented in LSDYNA [7].

Davison *et al.* [1] studied axisymmetric deformations caused by 62 and 124 μm fused silica particles impacting 2.54 mm thick fused silica mirrors at 6.2 and 9.9 km/s, respectively, and used the SPH and the Lagrangian cell methods in AUTODYN-2D. They used the Johnson-Holmquist (JH) material model [8], the maximum hydrostatic tensile stress equal to 130 MPa to delineate the spall failure, a polynomial equation of state (EoS), and the static damping feature in the hydrocode which decreases all velocities by a user defined factor after every time step. They found that the value of the maximum hydrostatic tensile stress at failure significantly affected the location and the time of formation of the detached spall in the vicinity of the crater.

For impact velocities varying from 2.67 to 4.24 km/s, Zhang *et al.* [9] experimentally studied HVI of 3.97 and 6.35 mm diameter aluminum alloy spheres on three glass/PVB laminated targets. They also employed the JH material model, a polynomial EoS, and the hydrocode AUTODYN to numerically study axisymmetric deformations of the system. They found that the PVB interlayer enhanced the protection provided by the glass sheet.

Michel *et al.* [4-6] experimentally and numerically studied the impact of steels pheres on glass targets. They used the SPH formulation implemented in the hydrocode LSDYNA [7], and found that the computed front and back surface spalls and perforation hole diameters were qualitatively similar to those observed in experiments, but their values were 34%, 32%, and 12%, respectively, lower than the average experimental values.

Here we use the SPH method implemented in AUTODYN [3] to study axisymmetric deformations caused by the impact of a steel sphere on a thin fused silica glass plate and employ the same geometric configurations and material models as those used by Michel *et al.* [4-6]. It is found that for various impact speeds, the presently computed fracture parameters in the glass target differ from their experimental and numerical values reported by Michel *et al.* Without having access to the source code, the differences in the two sets of numerical results can be attributed to either different choice of kernel functions in the two codes, the smoothing length, the volume assigned to each particle, the integration rule used to numerically evaluate various integrals, and different contact algorithms. We note that the classical SPH method exhibits tensile instability near the boundaries. Zhang and Batra [10] have successfully simulated the Taylor impact problem with the modified smoothed particle method (MSPH) that overcomes tensile instability and can have complete C^o basis functions of a desired order.

2. Problem Formulation

2.1 Problem Geometry

The configuration analyzed, depicted in Fig. 2, involves the impact at normal incidence of a 0.5 mm diameter steel sphere at the centroid of the top surface of a 2 mm thick and 40 mm diameter glass plate clamped at the periphery. The impactor and the target materials

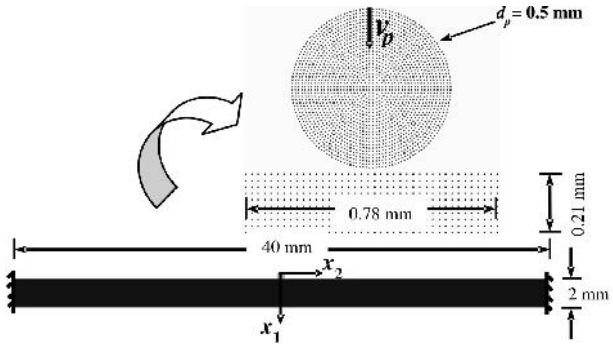

Fig. 2: Schematic sketch of the problem studied and a magnified view of the SPH particle distribution in the impacted region.

are assumed to be homogeneous and isotropic. For the glass we use the JH strength model and a polynomial EoS, and for the steel the Johnson-Cook (JC) material model and the Mie-Grüneisen EoS. Because of the symmetry in loading and geometry, it is reasonable to assume that deformations are axisymmetric about the axis of impact, i.e., the x_1-axis in Fig. 2. We thus impose x_2- (or radial) velocity = 0 and tangential tractions = 0 at points on the axis of symmetry all three components of velocity = 0 on the target mantle, and surface tractions = 0 on the remaining bounding surfaces of the steel sphere and the glass target except those contacting each other. The contact surface between the impactor and the target is assumed to be smooth. Thus at points on the contact surface the normal traction and the normal component of velocity are taken to be continuous, and the tangential traction = 0. We note that material points of the impactor and the target contacting each other vary with time. We use default values of the coefficients of the linear and the quadratic artificial viscosity, and do not use the static damping option in the hydrocode to reduce the kinetic energy of the system after every time step.

2.2 Material Model for Fused Silica

The polynomial EoS, Eqs. (1a) and (1b), the JH constitutive relation, Eq. (2), the JH damage model, Eq. (3), and the maximum tensile hydrostatic pressure criterion are used to simulate the hydrodynamic, the strength, the damage, and the spall failure in glass, respectively. Values of material parameters used to analyze the problem, taken from Ref. [11], are listed in Table 1 where μ is the shear modulus. These values, except for that of ρ_0 and μ, equal those used by Michel *et al.* [4-6] who took $\rho_0 = 2.53$ g/cm^3 and $\mu = 30.4$ GPa.

$$p = A_1\eta + A_2\eta^2 + A_3\eta^3 + \left(B_o + B_1\eta\right)\rho_o e, \ \eta \geq 0, \quad \text{(1a)}$$

$$p = C_1\eta + C_2\eta^2 + B_o\rho_o e, \ \eta \leq 0. \quad \text{(1b)}$$

In Eq. (1), $\eta = \rho/\rho_0 - 1$ is the compressive volumetric strain, ρ_0 the initial mass density, ρ the present mass density, e the internal energy density, and A_1, A_2, A_3, B_o, B_1, C_1 and C_2 are material constants. One can interpret A_1 and C_1 as the bulk modulus, K_o, at zero volumetric strain.

$$\sigma_D^* = \sigma_i^* - D\left(\sigma_i^* - \sigma_f^*\right), \qquad 0 \leq D \leq 1.0,$$

$$\sigma_i^* = \overline{A}\left(p^* + T^*\right)^{\overline{n}}\left(1 + \overline{C}\ln\dot{\varepsilon}_e^{*p}\right),$$

$$\sigma_f^* = Min\left[\left(p^*\right)^{\overline{m}}\left(1 + \overline{C}\ln\dot{\varepsilon}_e^{*p}\right)\overline{B}, \sigma_f^{*Max}\right]. \quad (2)$$

In Eq. (2), p^* and T^* are, respectively, the hydrostatic pressure, p, and the maximum tensile hydrostatic pressure normalized by the pressure at the Hugoniot elastic limit (HEL), p_{HEL}, σ_i^* the normalized equivalent stress, σ_f^* the normalized fracture strength, $\dot{\varepsilon}_e^{*p}$ the effective plastic strain rate normalized by the reference strain rate of 1.0 s^{-1}, σ_f^{*Max} the maximum fracture strength as a fraction of the intact strength $\overline{A}$, $\overline{C}$ the strain rate hardening parameter, $\overline{B}$ the fracture strength, and $\overline{m}$ and $\overline{n}$ are constants. The damage parameter D ($0 \leq D \leq 1$), calculated using Eqs. (3a) and (3b), reduces the material flow (or yield) stress from σ_i^* to σ_f^* with an increase in the value of D from 0 to 1.

$$D = \sum \frac{\Delta\varepsilon_e^p}{\varepsilon_f^p}, \quad \text{(3a)}$$

$$\varepsilon_f^p = D_1\left(p^* + T^*\right)^{D_2}, \quad \text{(3b)}$$

where $\Delta\varepsilon_e^p$ equals the effective plastic strain increment, ε_f^p is defined by Eq. (3b), and D_1 and D_2 are material parameters. The spall is assumed to initiate in the glass at the tensile hydrostatic pressure of 150 MPa. No erosion criterion is considered to delete the material.

For values of material parameters listed in Table 1, the Rayleigh wave speed in fused silica equals 2.18 km/s.

2.3 Material Model for Steel

The Mie-Grüneisen EoS, Eq. (4), and the JC relation, Eq. (5), are assumed for the steel projectile.

$$p=\frac{\rho_o c_b^2(\eta-1)\left[\eta-\frac{\Gamma_o}{2}(\eta-1)\right]}{\left[\eta-s_o(\eta-1)\right]^2}+\Gamma_o\rho_o c(\theta-\theta_o), \tag{4}$$

$$\sigma_y=\left[A+B\left(\varepsilon_e^p\right)^n\right]\left[1+C\ln\left(\frac{\dot{\varepsilon}_e^p}{\dot{\varepsilon}_o}\right)\right]\left[1-\left(\frac{\theta-\theta_o}{\theta_m-\theta_o}\right)^m\right]. \tag{5}$$

Here θ_0 is the temperature of a material point in the undeformed configuration, c the specific heat, c_b the bulk speed of sound, Γ_0 the Mie-Grüneisen parameter, and s_o the slope of the Hugoniot curve at the origin. In Eq. (4), the pressure is an affine function of the temperature rise. In Eq. (5), ε_e^p is the effective plastic strain, and $\dot{\varepsilon}_e^p$ the effective plastic strain rate, A the quasi-static yield stress, B and n strain hardening parameters, C and $\dot{\varepsilon}_o$ the strain rate hardening parameter and the nominal strain rate, respectively, θ_m the presumed melting temperature of the material, and m the thermal softening exponent.

The JC damage parameter, D, is obtained from Eq. (3a) by using Eq. (6) instead of Eq. (3b) to find ε_f^p, where ε_f^p is assumed to depend on the non-dimensional plastic strain rate, $\dot{\varepsilon}_e^p/\dot{\varepsilon}_o$, the temperature, and the stress triaxiality, p/σ_e.

$$\varepsilon_f^p=\left[d_1+d_2\exp\left(d_3\frac{p}{\sigma_e}\right)\right]\left[1+d_4\ln\left(\frac{\dot{\varepsilon}_e^p}{\dot{\varepsilon}_o}\right)\right]\left[1+d_5\left(\frac{\theta-\theta_o}{\theta_m-\theta_o}\right)\right], \tag{6}$$

$$\sigma_e=\sqrt{\frac{3}{2}s_{ij}s_{ij}}\,. \tag{7}$$

Here σ_e is the effective stress and s_{ij} a component of the deviatoric stress tensor.

Values of material parameters A, B, C, n, θ_m, m, and $d_1, d_2,\ldots, d_5$, taken from Refs. [12, 13], are listed in Table 2. Note that a positive value of p implies tensile pressure. Material points of the steel projectile are deleted from the analysis when D = 1.0.

3. Results

3.1 Effect of Particle Distributions

For impact velocity = 3 km/s and the initial kinetic energy of the steel sphere projectile = 2.29 J, we analyze deformations of the glass sheet by using three successively finer particle distributions for which the minimum radial distance between two adjacent particles in the steel sphere equals 10, 6 and 5.6 μm. The minimum distance in the corresponding particle distributions in the target equals 20, 14 μm, and 12.5 μm. One distribution of particles in a plane of the sphere passing through its center, and in the central target region is shown in Fig. 2.

For the three particle distributions and t = 30 μs we have exhibited in Fig. 3 the computed conchoidal diameters on the front and the back surfaces, D_{fs} and D_{bs}, and the hole-out diameter, D_c, for the glass target. The D_{fs} and D_{bs} are defined as the maximum diameter of the region spalled on the front and the back target surface, respectively. The D_c is defined only when there is complete perforation of the target, and it is taken to equal the diameter of the tunnel at the target mid-surface. Values of D_{fs}, D_{bs}, D_c and the minimum time step size, Δt_{min}, are listed in Table 3. These results suggest that values of D_{fs}, D_{bs}, and D_c for the 2nd particle distribution differ from those of the 3rd particle

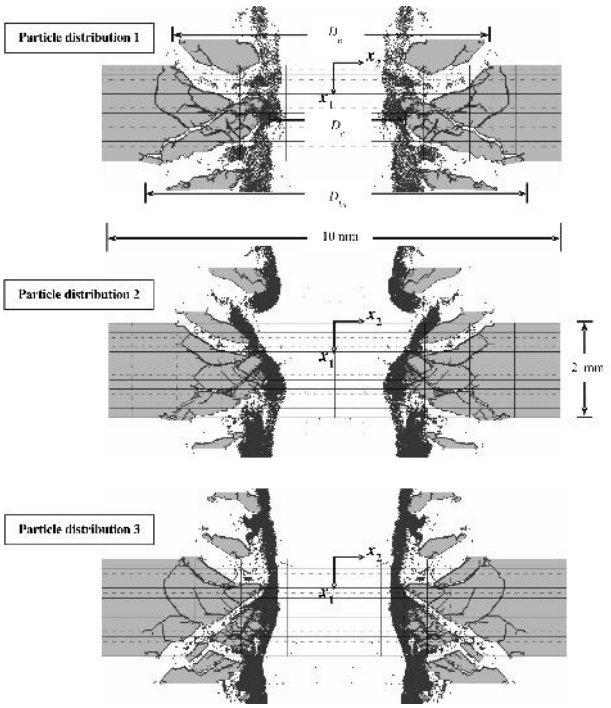

Fig. 3: At t = 30 μs, the 2 mm thick and the central 10 mm wide region showing deformed shape for the three successively refined particle distributions. The material in the gray coloured region has elastically deformed and that in the dark coloured region has spalled

distribution by 0.3%, 3.65%, and 0 %, respectively. Thus the 2nd particle distribution gives essentially converged values of D_{fs}, D_{bs} and $D_{c.}$

3.2 Elastic Wave Speeds and Impact Pressure

For values of material parameters listed in Tables 1 and 2, the theoretical longitudinal wave speed $c_l = (c_b^2 + 4/3\ c_s^2)^{1/2} = 6.21$ km/s and 5.43 km/s for the glass and the steel, respectively. Here $c_b^2 = A_1/\rho_0$ is the square of the bulk wave speed and $c_s^2 = \mu/\rho_0$ the square of the shear (or transverse) wave speed. The computed results indicate that the pressure wave reaches the back surface of the 2 mm thick glass target at about 0.32 μs giving the longitudinal wave speed from the computed results = 6.25 km/s for the glass which is very close to the theoretical value of 6.21 km/s.

The magnitude of the incident pressure, p_0, induced during the impact of two elastic bodies [14] is given by

Table 1: Values of material parameters for fused silica glass [11]

A_1 (GPa)	A_2 (GPa)	A_3 (GPa)	B_0	B_1	C_1 (GPa)
45.4	-138.0	290.0	0.0	0.0	45.4
C_2 (GPa)	$\overline{A}$ (GPa)	$\overline{B}$	$\overline{C}$	$\overline{n}$	$\overline{m}$
0.0	0.93	0.088	0.003	0.77	0.35
σ_f^{*Max}	D_1	D_2	ρ_0 (g/cm^3)	μ (GPa)	P_{HEL} (GPa)
0.5	0.053	0.85	2.23	27.9	2.92

Table 2: Values of material parameters for steel [12,13]

ρ_0 (g/cm^3)	c_b (km/s)	Γ_0	s_o	c (kJ/kg K)	A (GPa)
7.83	4.05	1.69	1.92	477.0	0.792
B (GPa)	C	n	m	θ_0 (K)	θ_m (K)
0.51	0.14	0.26	1.03	300	1793
$\dot{\varepsilon}_o$ (s^{-1})	d_1	d_2	d_3	d_4	d_5
1.0	0.05	3.44	-2.12	0.002	0.61
μ (GPa)					
77.0					

$$p_o = v_f \left(\frac{1}{\rho_o^f c_l^f} + \frac{1}{\rho_o^t c_l^t} \right)^{-1}, \tag{8}$$

where $\rho_0^{\,i}$ and $c_j^{\,i}$ ($i = f$ and t) are the initial mass density and the longitudinal wave speed, respectively. For values of material parameters assumed here, p_0 = 31.34 GPa which compares well with 32.83 GPa found from using the code. We note that this value of p_0 equals about 40 times the quasistatic yield stress of the steel and nearly equals the initial bulk modulus of fused silica.

3.3 Observation from the Numerical Solution

After closely studying computed results for the three particle distributions, we make the following general observations. Values of times listed below vary with the particle distribution and the number of particles used to analyze the problem.

- Crater lips start growing right after the impact.
- At about 0.4 μs, spallation initiates from a point on the axis of impact that is on the back surface of the silica plate and propagates radially. At approximately 0.6 μs a small region around the axis of impact whose thickness equals about 1/3rd of the target thickness has spalled. At t = 1 μs the spallation reaches the crater bottom and radial spall lines start emanating from points on the crater periphery. The average speed of propagation of spalled zone is 1.8 km/s which is less than the Rayleigh wave speed of 2.18 km/s in glass.
- At about 1.1 and 2.3 μs, respectively, two spall lines reach the front surface at x_2 = 1.89 and 3.44 mm. Similarly at 3.0, 3.3, 3.5, and 7 μs, respectively, four spall lines reach the back surface at x_2 = 2.08, 3.28, 3.58, and 4 mm.

The above-stated observations for the three particle distributions are summarized in Table 4.

Results depicted in Fig. 3 imply that when the particle distribution is successively refined, deformations of the target and the propagation of spall regions noticeably change. It is difficult to establish a convergence criterion for the computed results.

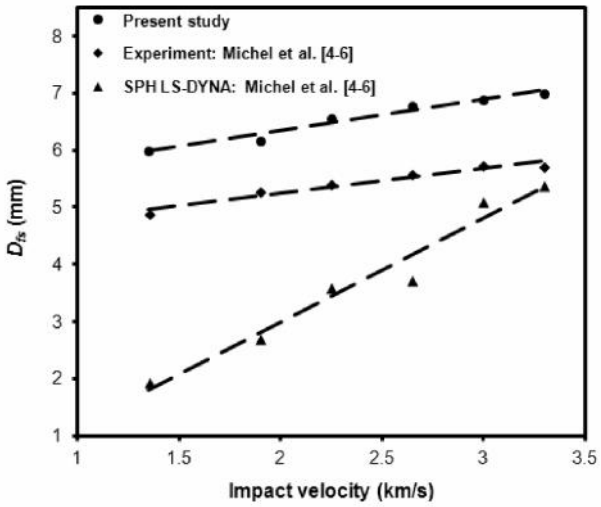

Fig. 4: Dependence of the front-surface conchoidal diameter upon the impact speed. Dashed lines are least-squares fit to the data and are guide to the eye

3.4 Results for Different Impact Velocities

For the problem studied in Section 3.1 and particle distribution 2, we compute values of the critical fracture parameters for impact speeds varying from

Table 3: Computed values of fracture parameters for the three particle distributions

Parameter/ particle distribution	Total No. of particles	Smoothing length* (μm)	Δt_{min} (ns)	Front-surface conchoidal dia., D_{fs} (mm)	Back-surface conchoidal dia., D_{bs} (mm)	Hole-out dia., D_c (mm)
1	100,958	10/20	0.65	6.88	8.3	2.8
2	207,035	6/14	0.36	6.74	7.9	2.6
3	259,090	5.6/12.5	0.28	6.72	8.2	2.6

* "/" separates smoothing length for the projectile and the target

Table 4: Summary of computed fracture patterns for the three particle distributions

	Front surface			Back surface		
Parameter/ particle distribution	No. of radial spall lines	Spall initiation time (μs)	Maximum radius of spalled region (mm)	No. of radial spall lines	Spall initiation time (μs)	Maximum radius of spalled region (mm)
1	2	1.1	2.04	4	0.4	2.75
2	2	1.1	2.07	4	0.4	2.65
3	2	1.1	2.06	4	0.4	2.8

1.35 to 3.3 km/s, and compare them in Figs. 4-6 with those experimentally and numerically found by Michel *et al*. [4-6]. The plots of the front-surface conchoidal diameters *versus* the impact speed depicted in Fig. 4 evinces that for the impact speeds considered, the present work and the numerical analysis of Michel *et al*. over-predict and under-predict, respectively, the conchoidal diameters than those found experimentally. However, both sets of numerical results for the back-surface conchoidal diameter are below the test values. The variation of the hole-out diameter with the impact speed exhibited in Fig. 6 suggests that the agreement between the experimental values and the two sets of numerically found values is better than that for the conchoidal diameters.

We have exhibited in Fig. 7 variation of the front-surface conchoidal diameter *versus* the impact energy. Eq. (9) is the least squares fit to the presently computed D_{fs} *vs*. E_k values where D_{fs} is in mm and E_k in Joules.

$$D_{fs} = 6.4012\ E_k^{0.0895} \tag{9}$$

We have compared values of D_{fs} calculated from scaling laws available proposed by Burt and Christiansen [19], Fechtig *et al*. [15, 16] and Yang *et al*. [20].

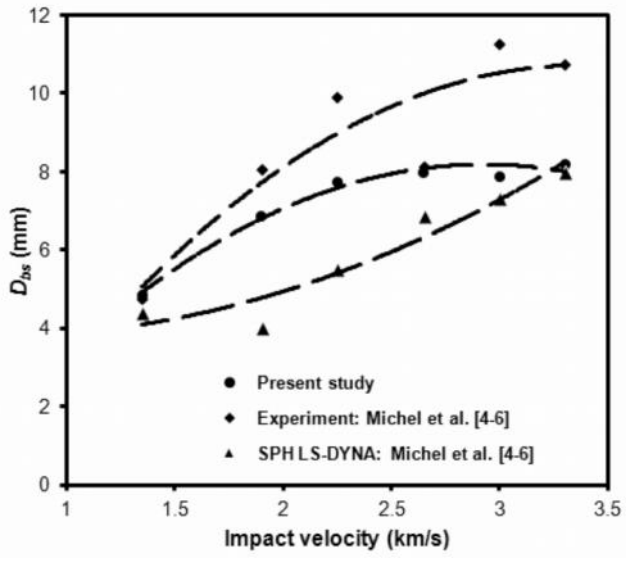

Fig. 5: Dependence of the back-surface conchoidal diameter upon the impact speed. Dashed lines are least-squares fit to the data and are guide to the eye

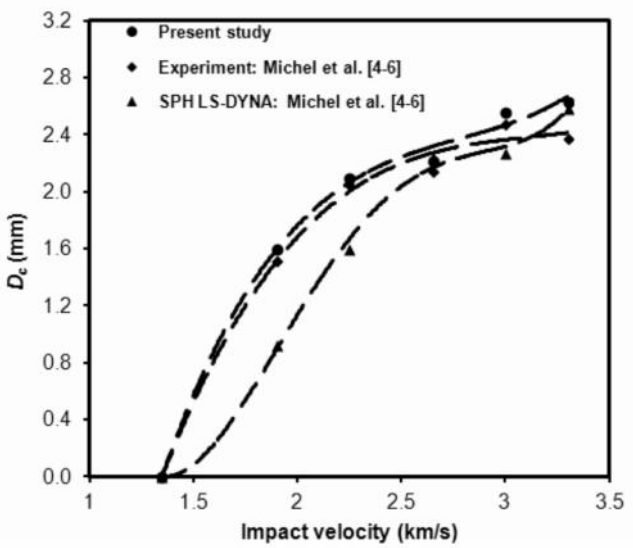

Fig. 6: Dependence of the hole-out diameter upon the impact speed. Dashed lines are least-squares fit to the data and are guide to the eye

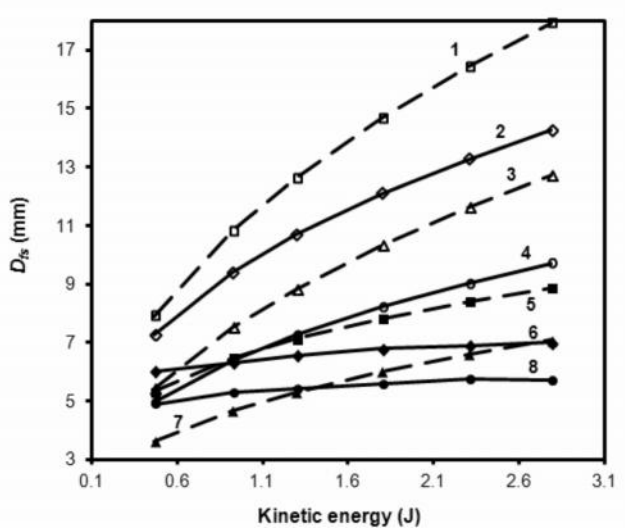

Fig. 7: Front-surface conchoidal diameter *vs* the impact energy from equations proposed by different investigators. Curve 1: Burt and Christiansen [19], curve 2: Fechtig *et al*. [15], curve 3: Schafer *et al*. [18], curve 4: Paul *et al*. [17], curve 5: Yang *et al*. [20], curve 6: present results represented by Eq. (9), curve 7: Fechtig *et al*. [16], and curve 8: Michel *et al*. [4-6]. Dashed and solid lines are guide to the eye

In Fig. 8, we have exhibited snap shots of the deformed shapes at 0.5, 1.5, 3, and 5 μs. The lengths of long and short spall radial lines as well as their numbers stabilize at about t = 3 μs even though the crater diameter and the crater depth continue to grow

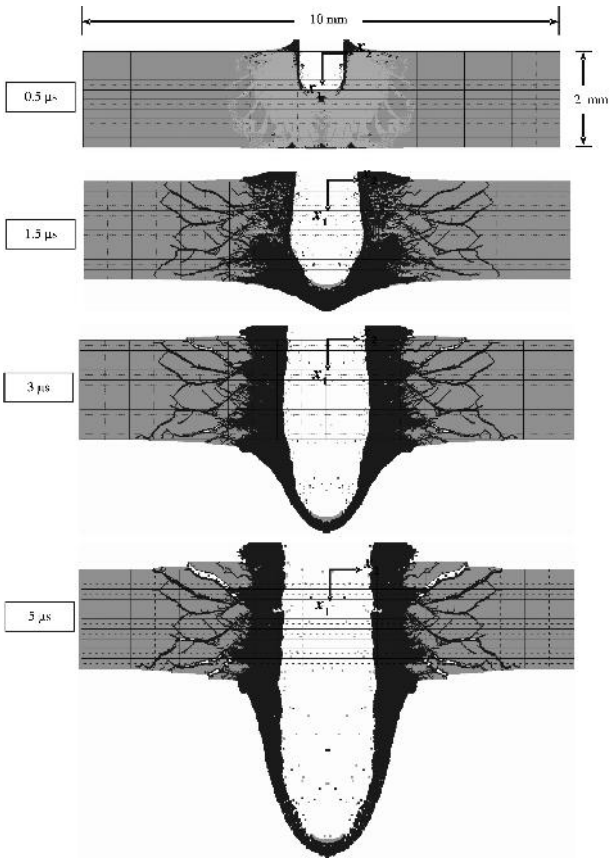

Fig. 8: For impact velocity = 3 km/s, snap shots of the deformed shape of the 2 mm thick and the central 10 mm wide region. The material in the gray colorued (light-gray in the Fig. at t = 0.5 μs) region has elastically (plastically) deformed and that in the dark colour has spalled

till about 3 and 5 μs, respectively. Particles above the top surface of the target are not displayed in these Figs.

4. Conclusions

We have used the smooth particle hydrodynamics formulation in the commercial software, AUTODYN, to study impact at normal incidence of a steel sphere on a fused silica sheet to delineate the effect of the impact speed on several fracture parameters such as the conchoidal diameters on the front and the back surfaces and the hole-out diameter. The steel has been modelled with the Johnson-Cook viscoplastic and damage relations. The response of fused silica has been simulated with the Johnson-Holmquist material and damage models, and the spall tensile hydrostatic pressure has been taken as 150 MPa.

It is found that the particle distribution and the number of particles strongly influence the fracture patterns and values of fracture parameters. Our results differ from those of Michel *et al.* [4-6] who used the SPH formulation in the commercial software, LSDYNA. These differences cannot be attributed to the slightly different values of the mass density and the shear modulus of glass in the two computations. Our analysis unlike that of Michel *et al.* over-predicts values of the front-surface conchoidal diameter and the hole-out diameter as compared to their corresponding experimental values. However, the present analysis like that of Michel *et al.* under-predicts back-surface conchoidal diameter than the corresponding experimental values. The difference between the computed and the test values varies with the impact speed. We have not investigated changing values of other material parameters to see if the agreement between the computed and the experimental values of fracture parameters can be improved.

5. Acknowledgement

Authors sincerely thank Prof. Dr. C Espinosa of Insitut Supérieur de l'Aéronautique et de l'Espace (ISAE/ DMSM), Toulouse, France, for providing values of material parameters of fused silica.

References

1. Davison D, Cour-Palais B G, Quan X, Holmquist T J, Cohen L M, Ramsey R and Cummings R *Int J Impact Eng* **29** (2003) 203-214
2. Cour-Palais B G *Int J Impact Eng* **5** (1987) 221-237
3. ANSYS/AUTODYN User manual and software **14** (2012)
4. Michel Y, Chevalier J M, Durin C, Espinosa C and Malaise F *Proc Hypervelocity Impact Symp* (2005)
5. Michel Y, Chevalier J M, Durin C, Espinosa C, Malaise F and Barrau J-J *Int J Impact Eng* **33** (2006) 441-451
6. Michel Y, Chevalier J M, Durin C, Espinosa C, Malaise F and Barrau J-J *J Phys IV France* **134** (2006) 1077-1083
7. LS-DYNA Keyword and theory manual **I** (1997)

8. Johnson G R and Holmquist T J *Proc American Inst of Phys Conf* **309** (1994) 981-984
9. Zhang W, Ha Y, Guan G and Pang B *Proc 4th European Conf Space Debris* (2005)
10. Zhang G M and Batra R C *J Comp Phys* **222** (2007) 374-390
11. Taylor A, Tsembelis K, Hayhurst C J, Kay L and Burchell M J *Int J Impact Eng* **23** (1999) 895-904
12. Johnson W H and Cook G R *Proc 7th Int Symp Ballistic* (1983)
13. Johnson W H and Cook G R *Eng Fract Mech* **2** (1985) 31-48
14. Chen X, Chandra N and Rajendran A M *Int J Solids Struct* **41** (2004) 4635-4659
15. Fechtig H, Hartung J B, Nagel K and Neukum G *Proc 5th Lunar Conf* (1974)
16. Fechtig H, Gentner W, Hartung J B, Nagel K, Neukum G, Schneider E and Storzer D *NASA SP*-370 (1974)
17. Paul K G, Igenbergs E B and Berthoud L *Int J Impact Eng* **20** (1997) 627-638
18. Schafer F K, Geyer T, Schneider E E, Rott M and Igenbergs E B *Int J Impact Eng* **26** (2001) 683-698
19. Burt R R and Christiansen E L *Int J Impact Eng* **29** (2003) 153-166
20. Yang J, Zhang J, Gong Z and Pang H *EPJ Web of Conf* **6** (2010).